Supplement of Clim. Past, 19, 2257–2286, 2023
https://doi.org/10.5194/cp-19-2257-2023-supplement

Supplement of

The Antarctic Ice Core Chronology 2023 (AICC2023) chronological framework and associated timescale for the European Project for Ice Coring in Antarctica (EPICA) Dome C ice core

Marie Bouchet et al.

Correspondence to: Marie Bouchet (marie.bouchet@lsce.ipsl.fr)

Supplementary Material

1. Study of the gas loss effect for the EDC $\delta O_2/N_2$ data

The EDC $\delta O_2/N_2$ data have been obtained from several measurement campaigns over the period 2005-2022 at LSCE. We detail in Table S1 the different conditions of storage and measurements of the series.

Table S1. Series of $\delta O_2/N_2$ obtained on the EDC ice cores with details on the storage and conditions of preparation.

Age range (AICC2012, ice age, ka BP)	Date of measurements	Bubbly or clathrate ice	Storage temperature since drilling	Analytical method	Reference
11.3 – 27.06	2006	Bubbly and bubble to clathrate	-20°C	Automated melt extraction line	This study
4.05 – 11.89 & 27.82 – 44.91	2008	Bubbly and bubble to clathrate	-20°C	Automated melt extraction line	This study
100.162 – 116.238	2010	Clathrate	-20°C	Automated melt extraction line	This study
121.19 – 151.32 & 237.7 – 260.27	2007	Clathrate	-20°C	Manual extraction line	This study
157.56 – 208.66	2017	Clathrate	-20°C	Automated melt extraction line	This study
193.14 – 229.19	2022	Clathrate	-20°C	Automated melt extraction line	This study
302.32 – 800	2005	Clathrate	-20°C	Manual extraction line (LSCE)	Landais et al. (2012)
459.77 – 800	2006	Clathrate	-20°C	Manual extraction line (LSCE)	Landais et al. (2012)
392.49 – 473.31	2007	Clathrate	-50°C	Manual extraction line (LSCE)	Landais et al. (2012)
700 – 800	2008	Clathrate	-50°C	Automated melt extraction line (LSCE)	Landais et al. (2012)
103.75 – 136.47 & 338.25 - 700	2012	Clathrate	-50°C	Automated melt extraction line (LSCE)	Bazin et al. (2016)
138.76 – 332.03	2016	Clathrate	-50°C	Automated melt extraction line (LSCE)	Extier et al. (2018b)
111.39 – 148.85 & 180.34 – 259.39 & 328.08 – 360.59 & 409.29 – 449.61 & 486.98 – 539.35	2020 - 2022	Clathrate	-50°C	Automated melt extraction line (LSCE)	This study

A correction has been applied on the datasets obtained in 2006 and 2007 because they were obtained on a new mass spectrometer. We found that the calibration of the $\delta O_2/N_2$ data at the time has not be done correctly when switching from the old to the new mass spectrometer and that a shift of +1.5 ‰ should be applied to the $\delta O_2/N_2$ data.

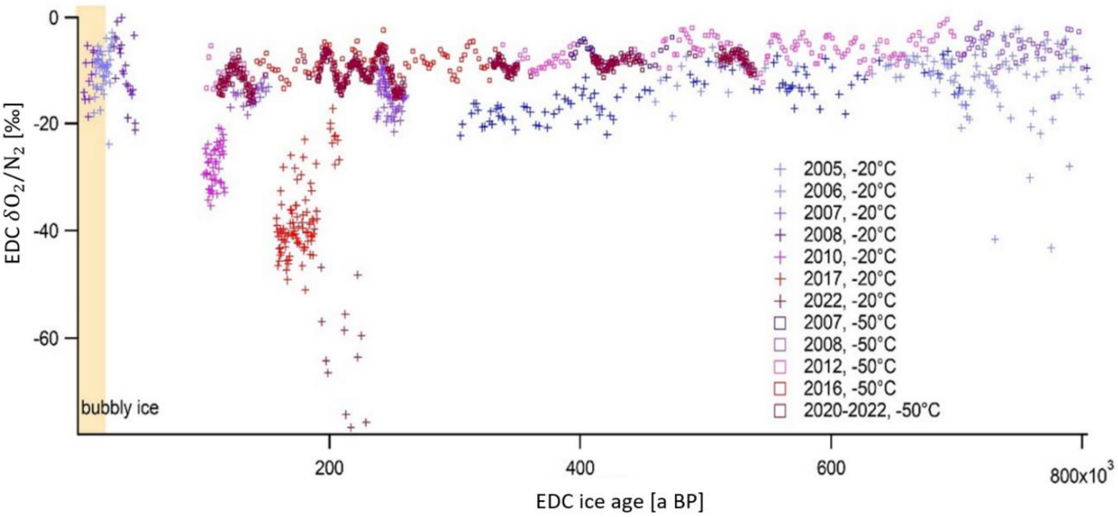

Figure S1. $\delta O_2/N_2$ series from the EDC ice core after different storage conditions. Note that the ice quality was very bad for the ice samples cut at the bottom of the ice core (corresponding to the age range of 800 – 700 ka BP). The orange rectangle frames the zone with only bubbly ice. The years of measurement are indicated and correspond to the different colors of the series.

Figure S1 shows the evolution of the mean level of $\delta O_2/N_2$ after different storage conditions. We do not notice differences in the $\delta O_2/N_2$ mean level for the samples stored at -50°C even after 14 years of storage (2022 vs 2008). This result is similar to the one obtained at Dome Fuji by Oyabu et al. (2021) even if we are working with smaller sample (20-30 g before removing the outer part). On the contrary, ice storage at -20°C has a strong effect, especially on clathrate ice. The samples analyzed in 2022 after storage at -20°C during more than 18 years exhibit $\delta O_2/N_2$ values as low as -80 ‰. The bubbly ice analyzed here has been stored at -20°C. The associated mean level of $\delta O_2/N_2$ is not significantly different from the one measured for samples stored at -50°C but the scattering is much larger as already observed on other series from bubbly ice (e.g. Oyabu et al., 2021).

2. Methods for aligning ice core records to reference curves

2.1 Study of the impact of filtering on $\delta O_2/N_2$ - insolation tie point identification

Figure S2 shows the smoothed $\delta O_2/N_2$ dataset using a low-pass (rejecting periods below 15 kyr) or a band-pass filter (keeping periods between 100 and 15 kyr periods, used by Bazin et al., 2013). The choice of filter does not alter the peak positions in the $\delta O_2/N_2$ curve

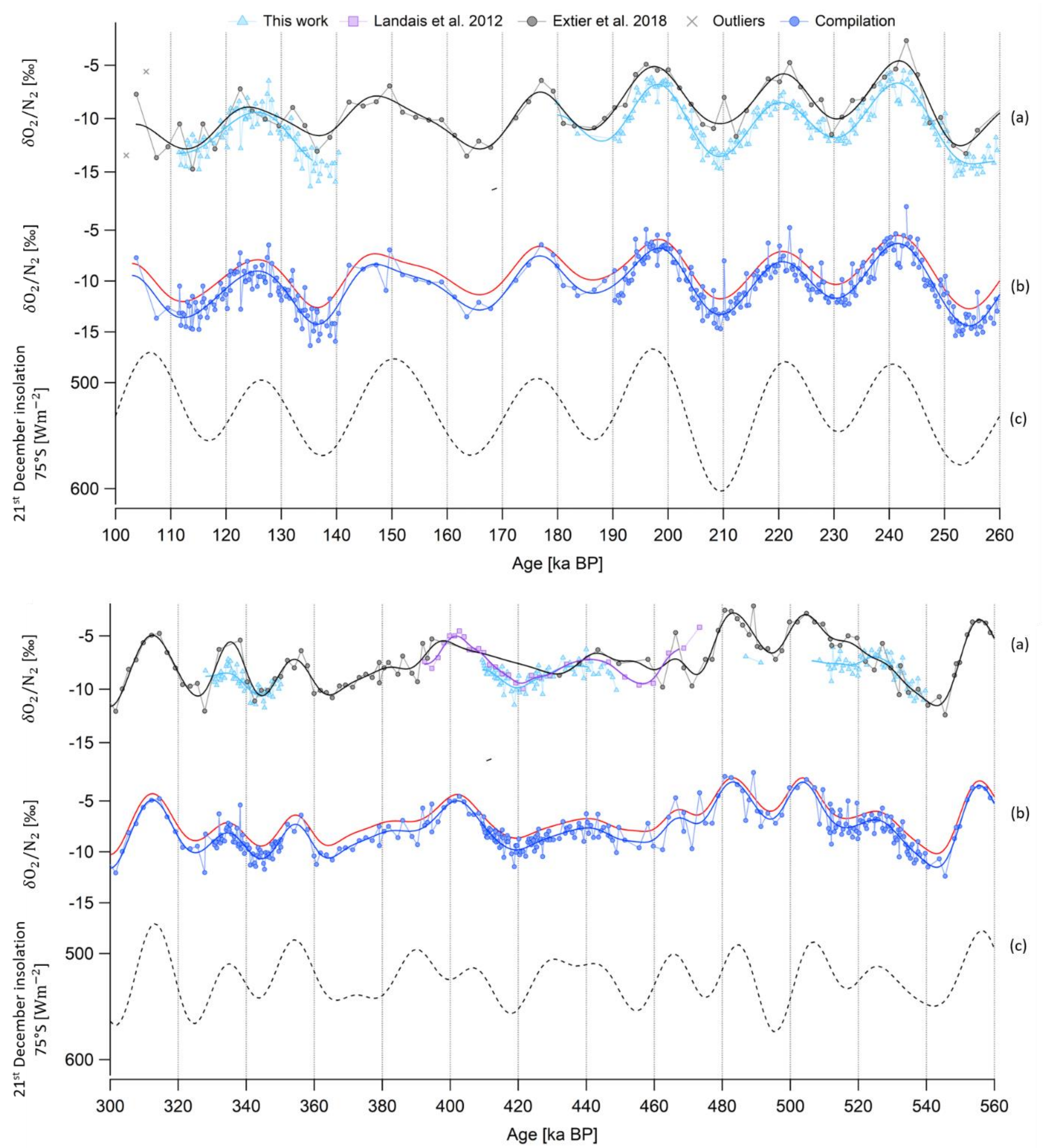

Figure S2. Evolution of EDC $\delta O_2/N_2$ record between 260 and 100 ka BP and between 560 and 300 ka BP. (a) EDC raw $\delta O_2/N_2$ old data between 800 and 100 ka BP (black circles for data of Extier et al., 2018b; and purple squares for data of Landais et al., 2012), outliers (grey crosses) and low-pass filtered signal (black and purple lines). EDC raw $\delta O_2/N_2$ new data (blue triangles, this study) and low-pass filtered signals (blue line). (b) Compilation of the two datasets and low-pass filtered (blue line) or band-pass filtered (red line) compiled signal. (c) 21st December insolation at 75° S on a reversed axis.

We compare tie point identification performed without (method a) and with (method b) filtering of the highly resolved $\delta O_2/N_2$ record between 260 and 180 ka BP (Fig. S3). The signal is first interpolated every 100 years. For the method a, we identified the mean maximum (or minimum) position $\text{age}_{\max(i),\text{a}}$ (or $\text{age}_{\min(i),\text{a}}$) as the middle of the age interval $[x_1; x_2]$ in which $\delta O_2/N_2$ is superior (or inferior) to a certain threshold. The threshold is defined as 95 % (or 5 %) of the amplitude difference D_i between the considered maximum and the minimum immediately preceding it (or between the considered minimum and the maximum immediately following it). The process is reiterated every ~10 kyr (precession half period) when an extremum is reached in the $\delta O_2/N_2$ signal. For the method b (described in the main text), we detected the peak positions ($age_{max(i),b}$ and $age_{min(i),b}$) in the $\delta O_2/N_2$ via an automated method using the zero values of the time derivatives of the low-pass filtered $\delta O_2/N_2$ compiled signal. After comparison of the peak positions identified by methods a and b (Table S2), we found an average disagreement of 700 years, with the largest value, 2150 years, observed between $age_{min(i+1),b}$ and $age_{min(i+1),a}$ at about 230 ka BP (Fig. S3). This period coincides with abrupt variations in the EDC δD record (Fig. S3), reflecting changes in surface climatic conditions which may have impacted high resolution variability of the $\delta O_2/N_2$ signal in addition of the insolation effect. Over periods of lower resolution of the $\delta O_2/N_2$ signal, the extrema positions are not affected by the filtering by more than 600 years (Table S2).

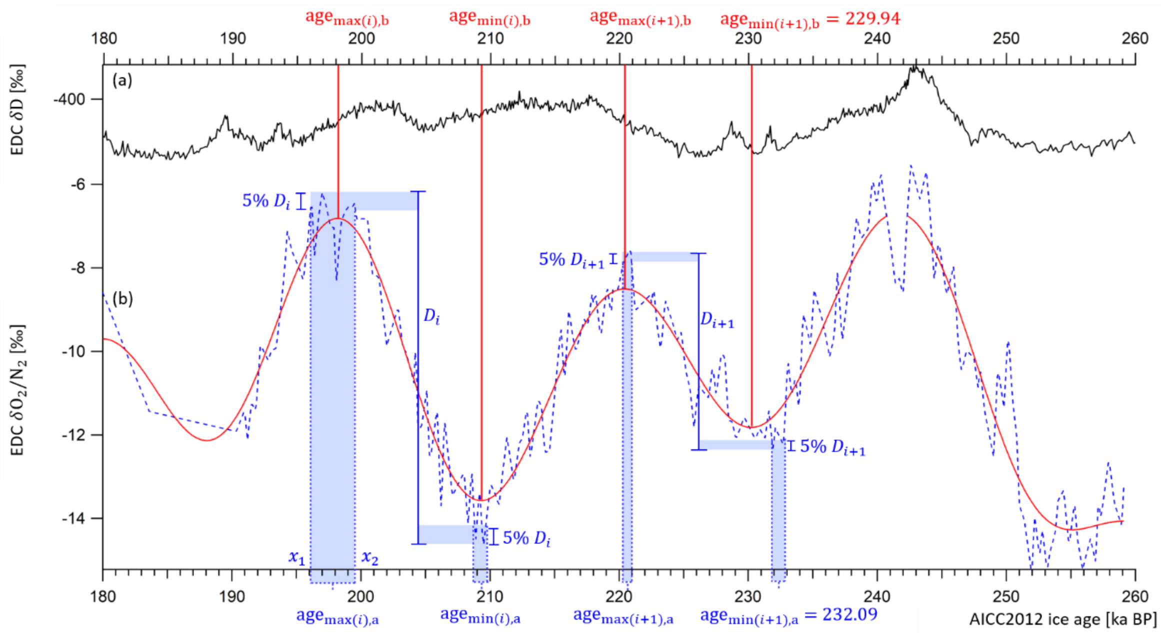

Figure S3. Identification of peaks position in filtered or unfiltered $\delta O_2/N_2$ record between 260 and 180 ka BP. (a) EDC δD (Jouzel et al. 2007). (b) EDC $\delta O_2/N_2$ (blue dashed curve) and low-pass filtered EDC $\delta O_2/N_2$ (red curve). Peaks position in the $\delta O_2/N_2$ record is identified as per methods a or b. Following the method a, the maximum position $age_{max(i),a}$ (on the bottom horizontal axis) is the middle of the age interval $[x_1; x_2]$ (blue vertical rectangles) in which $\delta O_2/N_2$ values are superior to 95 % of the difference D_i (vertical blue bars). The other peaks position is indicated in a similar way on the bottom horizontal axis. Following the method b, the extremum position is given by a 0 value in the temporal derivative of the filtered $\delta O_2/N_2$ record. The peak positions obtained with the method b ($age_{max(i),b}$, $age_{min(i),b}$) are indicated by red vertical bars and displayed on the top horizontal axis.

Table S2. Peak positions of $\delta O_2/N_2$ identified as per method a and method b between 260 and 180 ka BP. The age difference found between methods a and b is calculated. The average age difference is of 700 years and the standard deviation is of 250 years. EDC ice age as per AICC2012 and orbital ages as per Laskar et al. 2004.

Peak position (ka BP)			**Age difference (years)**
Method a	Method b	Insolation	Between methods a and b
197.64	197.94	196.8	300
209.19	209.14	210.1	50
220.69	220.24	220.8	450
232.09	229.94	231.7	2,150

241.84	241.24	240.1	600
			Average: 700
			Standard deviation: 250

2.2 Aligning EDC $\delta^{18}O_{atm}$ record and climatic precession variations

For the construction of the new AICC2023 chronology between 800 and 590 ka BP, the EDC $\delta^{18}O_{atm}$ record is aligned with the climatic precession delayed or not by 5,000 years depending on the occurrence of Heinrich like events, reflected by peaks in the IRD record from the North Atlantic Ocean (Sect 3.2.3 in the main text). Potential errors may arise from aligning $\delta^{18}O_{atm}$ to precession (Oyabu et al., 2022). To support the use of our approach, we test three methodologies to align $\delta^{18}O_{atm}$ and precession. Four test chronologies are built:

1) The test chronology 1 is obtained by aligning $\delta^{18}O_{atm}$ to 5-kyr-delayed precession as in Bazin et al. (2013).
2) The test chronology 2 is obtained by aligning $\delta^{18}O_{atm}$ to precession as it would be expected if only precession is driving the $\delta^{18}O_{atm}$ signal.
3) The test chronology 3 is obtained by aligning $\delta^{18}O_{atm}$ to precession delayed if IRD counts are superior to 10 counts g^{-1} and to precession without delay if IRD counts are inferior to 10 counts g^{-1}.
4) The test chronology 4 is obtained by matching $\delta^{18}O_{atm}$ and $\delta^{18}O_{calcite}$ variations only.

2.2.1 Between 810 and 590 ka BP

We first evaluate the impact on the chronology whether $\delta^{18}O_{atm}$ is aligned with the precession with or without delay between 810 and 590 ka BP. The age mismatch between test chronologies 1 and 2 is of 3,000 years on average, reaching its maximum value of 3,700 years at 712 $\pm$ 2.6 ka BP (red arrow in Fig. S4).

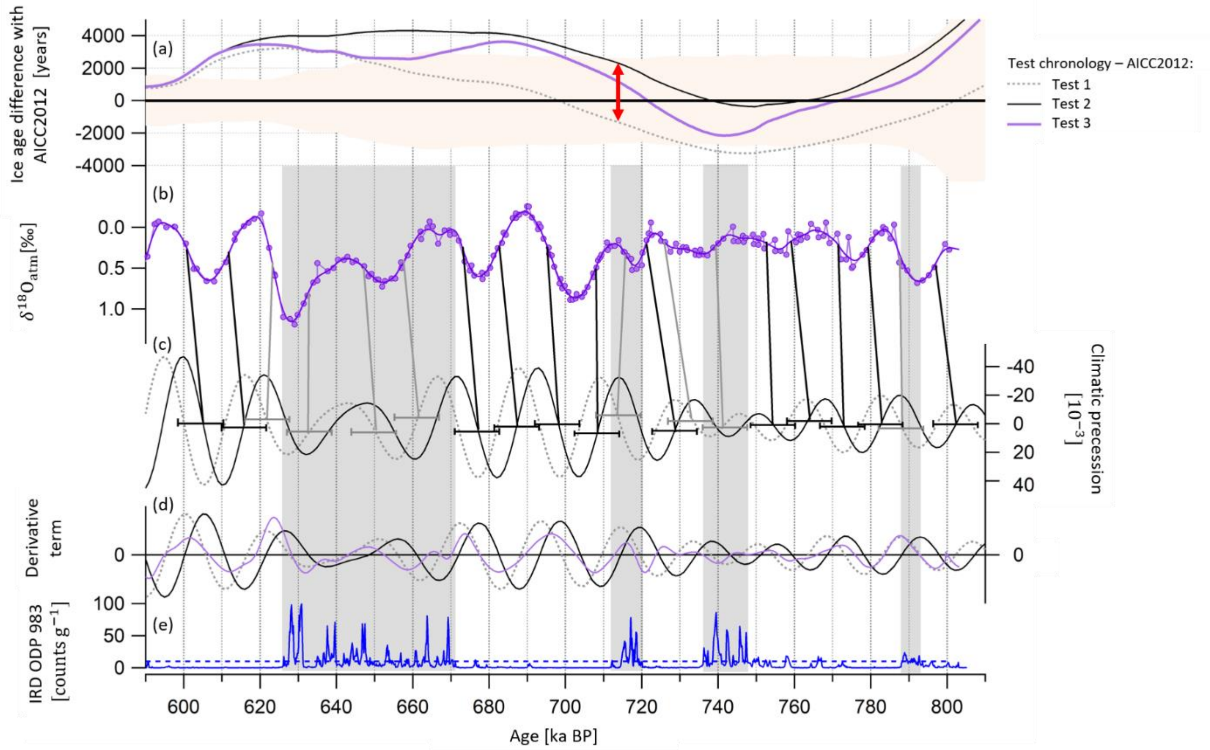

Figure S4. Alignment of EDC $\delta^{18}O_{atm}$ and climatic precession and impact on the chronology between 810 and 590 ka BP. (a) EDC ice age difference between AICC2012 and three test chronologies (1) test chronology 1 (grey dotted line), (2) test chronology 2 (black dashed line), (3) test chronology 3 (purple plain line). AICC2023 ice age 1σ uncertainty is shown by the orange area. The largest age difference between chronology 1 and 2 is indicated by the red arrow at 712.0 ± 2.6 ka BP. (b) Compiled EDC $\delta^{18}O_{atm}$ (purple circles). (c) Precession delayed by 5 kyr (grey dotted line) and not delayed (black dashed line) (Laskar et al. 2004). (d) Temporal derivative of precession (black dashed line), delayed precession (grey dotted line) and of the compiled $\delta^{18}O_{atm}$ record (purple plain line). (e) IRD (red by McManus et al. 1999; blue by Barker et al. 2019, 2021). The gray squares indicate periods where IRD counts are superior to the 10 counts g^{-1} threshold shown by the blue dotted horizontal line. Grey vertical bars illustrate new tie points between EDC $\delta^{18}O_{atm}$ and delayed precession mid-slopes (i.e. derivative extrema) when IRD counts are superior to the threshold. Black vertical bars illustrate new tie points between EDC $\delta^{18}O_{atm}$ and precession mid-slopes (i.e. derivative extrema) when no Heinrich-like events is shown by IRD record. The 12 kyr 2σ-uncertainty attached to the tie points is shown by the horizontal error-bars in panel b.

2.2.2 Between 300 and 100 ka BP

Then, we test the three methodologies to align $\delta^{18}O_{atm}$ and precession over the 100-300 ka period, where we have high confidence in our chronology.

Over this time interval, the test chronology 3 appears to be the best compromise as it agrees well with both the AICC2023 age model and the chronology derived from $\delta^{18}O_{atm}$-$\delta^{18}O_{calcite}$ matching (Fig. S5). This is why we believe that it can faithfully be applied to the bottom part of the EDC ice core while keeping large uncertainties in the tie points (1σ uncertainty of 6 kyr).

This agreement is particularly satisfying over the 120-160 ka BP time interval. Over this period, Oyabu et al. (2022) identified a large peak (up to 61%) in the IRD record of McManus et al. (1999) (red plain line in panel e) corresponding to HE 11 between 131 and 125 ka BP. Yet, if we consider the IRD record of Barker et al. (2019,

2021) used in our study because it covers the last 800 kyr (blue plain line in panel e), we observe another large peak (up to 56 counts g^{-1}) at around 150-156 ka BP. Because of this presence of IRD, to establish the test chronology 3, we tuned $\delta^{18}O_{atm}$ to the 5-kyr delayed precession over the whole period stretching from 155 to 124 ka BP (gray frame), which is larger than the duration covering only HE 11.

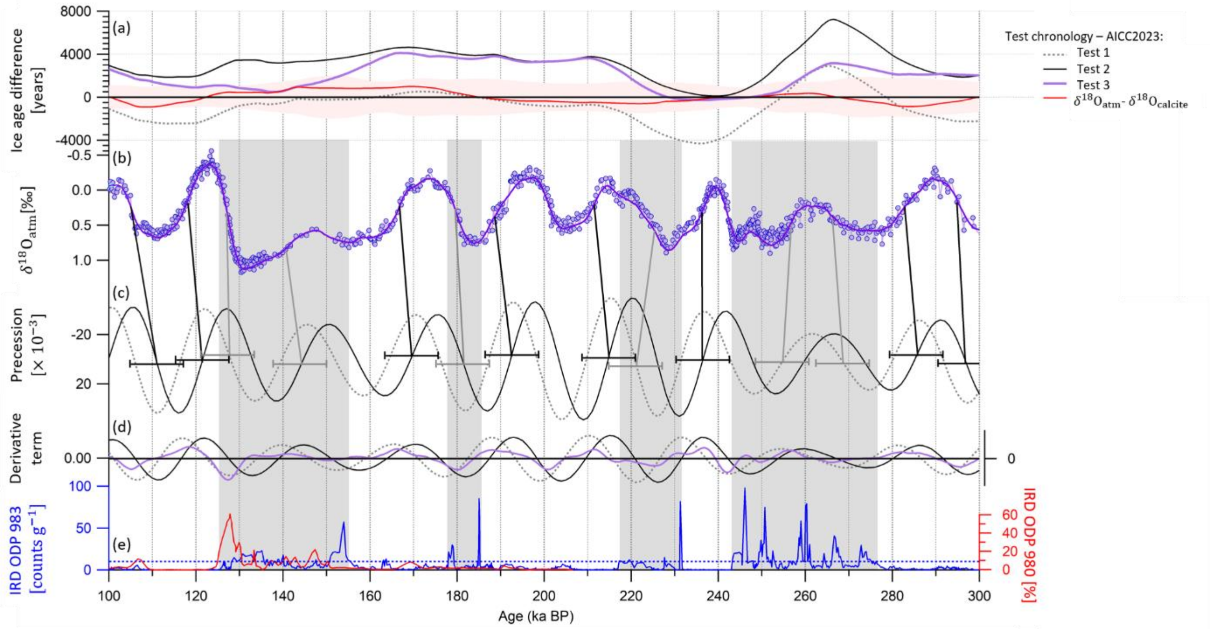

Figure S5. EDC ice age difference between test chronology and AICC2023 between 300 and 100 ka BP. (a) EDC ice age difference between AICC2023 and 4 tests chronologies: (1) test chronology 1 (grey dotted line), (2) test chronology 2 (black dashed line), (3) test chronology 3 (purple plain line) and (4) test chronology 4 derived using only $\delta^{18}O_{atm}$-$\delta^{18}O_{calcite}$ matching (red plain line). AICC2023 ice age 1σ uncertainty is shown by the red area. (b) $\delta^{18}O_{atm}$ data from EDC (purple circles) and Vostok (blue circles). (c) Precession delayed by 5 kyr (grey dotted line) and not delayed (black dashed line) (Laskar et al. 2004). (d) Temporal derivative of precession (black dashed line), delayed precession (grey dotted line) and of the compiled $\delta^{18}O_{atm}$ record (purple plain line). (e) IRD (red by McManus et al. 1999; blue by Barker et al. 2019, 2021). The gray squares indicate periods where IRD counts are superior to the 10 counts g^{-1} threshold shown by the blue dotted horizontal line. Grey vertical bars illustrate new tie points between EDC $\delta^{18}O_{atm}$ and delayed precession when IRD counts are superior to the threshold. Black vertical bars illustrate new tie points between EDC $\delta^{18}O_{atm}$ and precession when no Heinrich-like event is shown by IRD record. The 12 kyr 2σ-uncertainty attached to the tie points is shown by the horizontal error-bars in panel b.

3. Sensitivity tests on background scenarios and associated relative uncertainties

3.1 Background lock-in-depth (LID) scenario at Dome C

The background LID scenario can be derived either from the $\delta^{15}N$ data (i.e. experimental LID), or from firn modeling (i.e. modeled LID). We favor the use of $\delta^{15}N$ data when there are available. Over depth intervals where no measurements of $\delta^{15}N$ were made, the LID can be deduced from firn modeling or from a synthetic $\delta^{15}N$ record using the δD-$\delta^{15}N$ relationship (Bazin et al., 2013). In this work, we assess the credibility of three composite LID scenario (Table S3) constructed using the firn model (Bréant et al., 2017) or the synthetic $\delta^{15}N$ record when no data are available. The credibility is defined by the criterion Δ as per:

$$\Delta = \overline{|(\text{analyzed LID } - \text{background LID})|}$$

Δ represents the average absolute value of the mismatch between the background LID (i.e. prior LID provided in input in Paleochrono) and analyzed LID (i.e. the posterior LID given by Paleochrono) scenarios of LID. The weaker is Δ, the closer the background scenario is to the analyzed scenario, meaning that the background scenario is in relatively good agreement with chronological information compelling the inverse model in Paleochrono. On the contrary, the larger is Δ, the more Paleochrono is forced to significantly modify the background scenario which is incompatible with the chronological constraints. Therefore, the larger Δ is, the less credible is the prior LID scenario. It should be noted that the relative error in the prior LID scenario and the age constraints input in Paleochrono are equal in each test, so that the mismatch Δ is only impacted by the value of the prior LID from one test to another. Three background scenarios of LID are tested (Table S3).

Table S3. Test of three composite background LID scenarios. Test A corresponds to the background LID used to constrain AICC2012 chronology. Test B corresponds to the background LID used in the new AICC2023 chronology. Configuration 1 implies consideration of impurity concentration in the firn model. Configuration 2 implies **no** consideration of impurity concentration in the firn model.

	Test			**δ^{15}N data availability**	**Depth interval (m)**
	A (AICC2012)	B (AICC2023)	C		
LID calculation	From raw δ^{15}N data assuming a negligible thermal signal.	From δ^{15}N data corrected for thermal fractionation estimated by the firn model (configuration 1).	From δ^{15}N data corrected for thermal fractionation estimated by the firn model (configuration 2).	Yes	[345 – 578], [1086 – 1169] and [1386 – bottom]
	From δ^{15}N synthetic record (using the δD-δ^{15}N relationship).	From firn modeling (configuration 1)	From firn modeling (configuration 2)	No	[0 – 345], [578 – 1086] and [1169 – 1386]

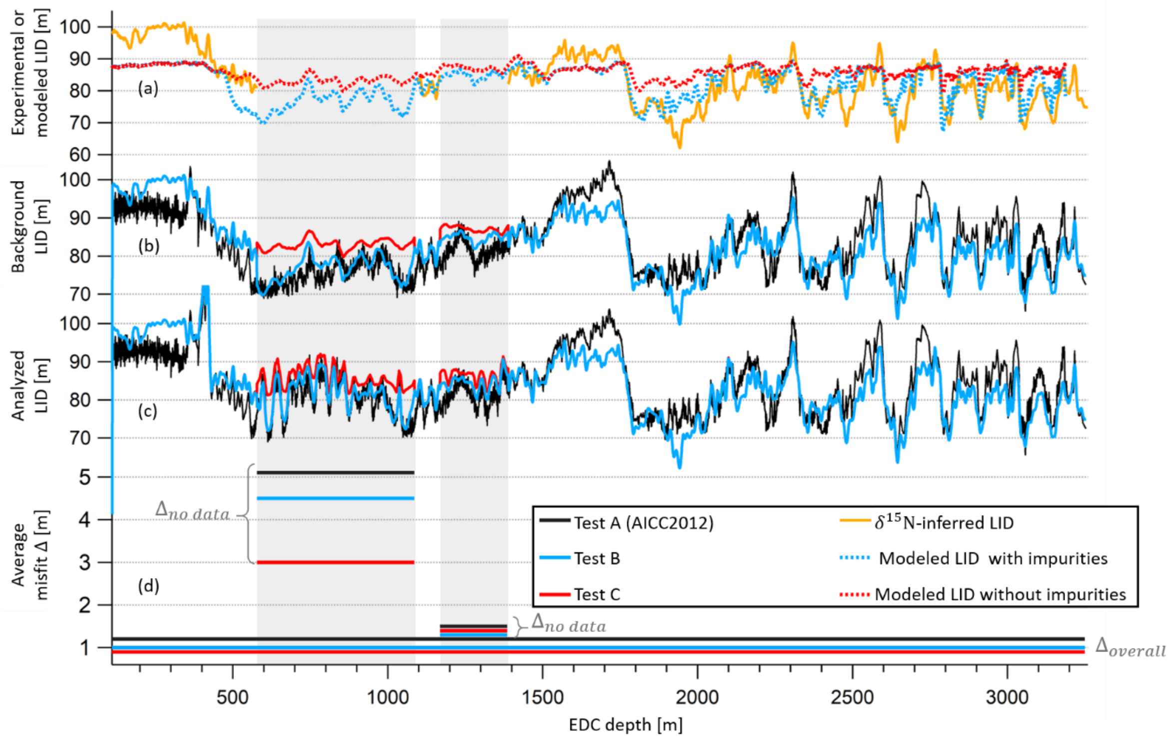

Figure S6. Mismatch Δ between background and analyzed LID for EDC over the 100-3200 m depth interval. (a) Experimental LID (orange) and modeled LID scenarios as per configuration 1 (with impurities, blue dots) and configuration 2 (without impurities, red dots). (b) Composite background LID as per tests A (black), B (blue) and C (red). (c) Analyzed LID scenarios given by Paleochrono. (d) Three values of the misfit Δ are calculated for the three composite LID: $\Delta_{no\ data}$, averaged over the two depth intervals where δ^{15}N data are not available (either between 578 and 1086 m or between 1169 and 1386 m, see intervals shown by grey rectangles), and $\Delta_{overall}$, averaged over the whole 3200 m.

For the construction of the AICC2012 timescale, the background LID scenario at EDC was derived from a synthetic δ^{15}N record using the δD-δ^{15}N relationship (Bazin et al., 2013). Yet, this scenario (A, Table S3) is associated with the largest mismatch criterion over the last 800 kyr, reaching Δ = 5 m over the 578-1086 m depth interval where no δ^{15}N data are available (Fig. S6). Hence it is believed to be the least pertinent among the three tested scenarios and we decided not to use the δD-δ^{15}N relationship to construct the prior LID scenario in this work.

Modeled LID scenarios (B and C, Table S3) are characterized by smaller mismatch criteria Δ than LID A regardless of the depth interval considered (Fig. S6), hence we believe that firn modeling estimates reproduce well the evolution of past LID at EDC site. In the firn model, the creep factor can be either dependent on impurity inclusion inducing firn softening (giving LID B) or not (giving LID C). The LID sensitivity to the impurity parameter is evaluated by comparing LID B and LID C performances. Even though LID B is associated with a smaller criterion Δ between 578 and 1086 m, LID B and LID C show comparable values for Δ over the last 800 kyr (Fig. S6). Bréant et al. (2017) argued that implementing the impurity dependence in the model reduces the δ^{15}N data-model mismatch at Dome C. This is particularly verified over deglaciations where significant LID augmentations inferred from δ^{15}N are well reproduced by the modeled LID when the impurity parameter is included (panel a in Fig. S6). We thus follow the recommendation of Bréant et al. (2017) and use the composite LID B scenario to constrain the new AICC2023 chronology.

Discontinuities are visible when switching from experimental to modeled values when no data are available (grey rectangles on Fig. S7). To avoid these discontinuities, we test a LID scenario where the modeled LID is fitted to experimental LID values (orange curve in Fig. S7). In other words, the firn modeling estimates are adjusted, by standard normalization, to the scale of LID values derived from $\delta^{15}N$ data. Adjusting the modeled LID to experimental LID values induces a modification of 4.7 m at most (see red arrow) which remains within the background relative uncertainty (20%).

On the depth interval from 578 to 1086 m, the modeled scenario without any fitting to $\delta^{15}N$-inferred LID (blue curve, Fig. S7) is almost as effective as the one that was fitted (orange curve, Fig. S7) (i.e., close Δ values). On the second depth interval of interest, from 1169 to 1386 m, both scenarios show equal Δ values.

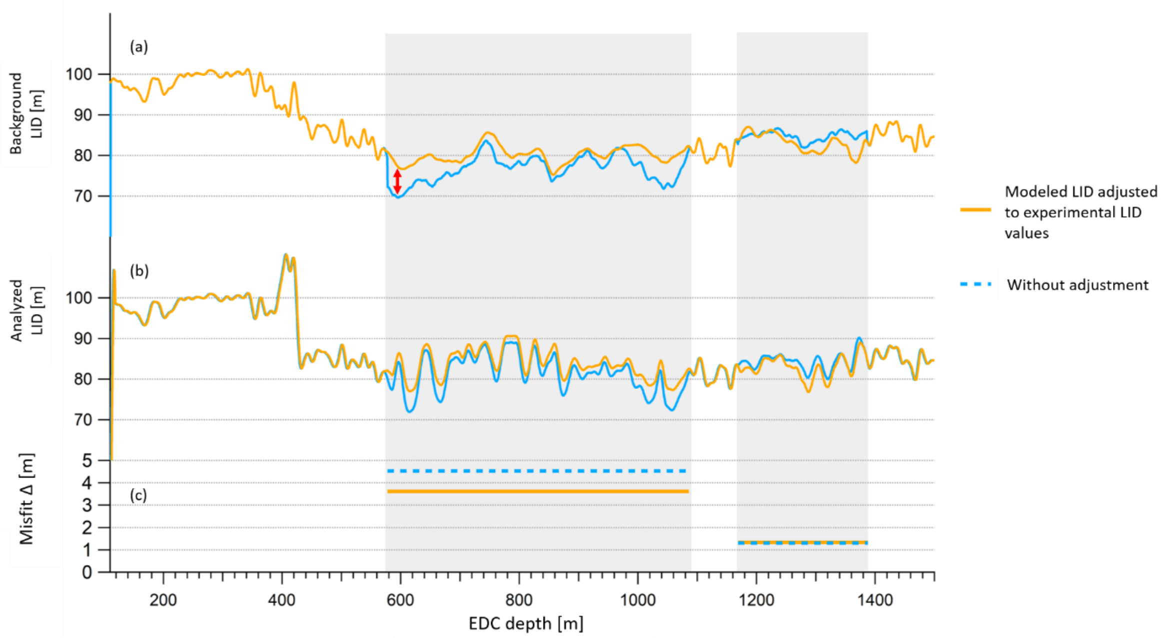

Figure S7. Mismatch Δ between background and analyzed LID for EDC over the 100-1500 m depth interval. (a) Background LID with and without adjusting the modeled LID to experimental LID values (orange and blue curves respectively). (b) Analyzed LID. (c) The averaged value of the misfit, Δ, is calculated for the two LID over the two depth intervals where $\delta^{15}N$ data are not available (either between 578 and 1086 m or between 1169 and 1386 m, see intervals shown by grey rectangles).

We thus conclude that we can keep the scenario combining $\delta^{15}N$-inferred LID and modeled LID in the construction of AICC2023.

3.2 Background uncertainties for LID, accumulation rate and thinning scenarios

Although there is no objective way to assign specific prior uncertainties, the values chosen by Bazin et al. (2013) seem unrealistic (i.e. 80 % of uncertainty for the LID during some glacial periods at EDC whereas firn modeling and $\delta^{15}N$ agree within a 20 %-margin at most). That is why we believe the prior uncertainties should be reduced in AICC2023 and implement the following major changes (blue plain line in Fig. S8 and S9):

- The LID background relative uncertainty is reduced to values oscillating between 10 and 20 % at most, excluding values reaching 80 % used in AICC2012. The reason for this modification is that in 2012, the mismatch between firn model outputs and δ^{15}N-inferred LID was not understood. In the meantime, much progresses have been made, confirming that the δ^{15}N-inferred LID was correct and firn models or their forcing have been adapted (Parrenin et al., 2012; Bréant et al., 2017; Buizert et al., 2021).
- The thinning relative uncertainty is evolving linearly, rather than exponentially as it was done in AICC2012. The linear uncertainty permits to have a significant uncertainty at intermediate depth levels while with the exponential shape, the uncertainty was essentially located at lower depth levels, which was not realistic.
- The accumulation relative uncertainty is decreased to 20 %, as opposed to 60 % used in AICC2012. This choice is motivated by the study of Parrenin et al. (2007) who counted event duration in EDC and DF ice cores and found out an offset of 20 % on average.

We build different test chronologies by keeping the same age constraints and background scenarios as in AICC2023 but varying the background errors (Table S4). The largest age offset is observed between the test AICC2012 and the other test chronologies at around 650 ka BP. It reaches 400 years (see red arrow in Fig. S8), which is not significant considering the uncertainty associated with the test chronologies over this period (ranging from 1,800 to 3,400 years). Since varying the background uncertainties has no significant impact on the final age model and the background uncertainties of AICC2012 seem unrealistic, we reduce the background errors with respect to AICC2012 and we use the Test 5 configuration from Table S4 to construct AICC2023.

Table S4. The different prior relative uncertainties tested for LID, thinning and accumulation. The LID prior relative uncertainty is set between 0.1 or 0.2 whether δ^{15}N data are available or not.

Test	Sites	LID	Thinning	Accumulation
Test AICC2012	EDC	From AICC2012 (Bazin et al., Veres et al., 2013)		
	EDML			
	VK			
	TALDICE			
	NGRIP			
Test 0	EDC	0.1 (data) or 0.2 (no data)	Linear from 0 to 0.5	0.2
	EDML	0.1 (data) or 0.2 (no data)	Linear from 0 to 0.5	From AICC2012 (between 0.2 and 0.8)
	VK	0.1 (data) or 0.2 (no data)	Linear from 0 to 0.5	Linear from 0.2 to 0.7
	TALDICE	0.2	From AICC2012 (exponential from 0 to 2.4)	0.2
	NGRIP	0.2	Linear from 0 to 0.5	0.2
Test 1	EDC	0.1 (data) or 0.2 (no data)	Linear from 0 to 0.5	0.2
	EDML	0.1 (data) or 0.2 (no data)	Linear from 0 to 1	From AICC2012 (between 0.2 and 0.8)
	VK	0.1 (data) or 0.2 (no data)	Linear from 0 to 0.5	Linear from 0.2 to 0.7
	TALDICE	0.2	From AICC2012	0.2

			(exponential from 0 to 2.4)	
	NGRIP	0.2	Linear from 0 to 0.5	0.2
Test 2	EDC	0.1 (data) or 0.2 (no data)	Linear from 0 to 0.5	0.2
	EDML	0.1 (data) or 0.2 (no data)	Linear from 0 to 0.5	0.2
	VK	0.1 (data) or 0.2 (no data)	Linear from 0 to 0.5	Linear from 0.2 to 0.7
	TALDICE	0.2	From AICC2012 (exponential from 0 to 2.4)	0.2
	NGRIP	0.2	Linear from 0 to 0.5	0.2
Test 3	EDC	0.1 (data) or 0.2 (no data)	Linear from 0 to 0.5	0.2
	EDML	0.1 (data) or 0.2 (no data)	Linear from 0 to 1	0.2
	VK	0.1 (data) or 0.2 (no data)	Linear from 0 to 0.5	Linear from 0.2 to 0.7
	TALDICE	0.2	From AICC2012 (exponential from 0 to 2.4)	0.2
	NGRIP	0.2	Linear from 0 to 0.5	0.2
Test 4	EDC	0.1 (data) or 0.2 (no data)	Linear from 0 to 0.5	0.2
	EDML	0.1 (data) or 0.2 (no data)	Linear from 0 to 0.5	Linear from 0.2 to 0.7
	VK	0.1 (data) or 0.2 (no data)	Linear from 0 to 0.5	Linear from 0.2 to 0.7
	TALDICE	0.2	From AICC2012 (exponential from 0 to 2.4)	0.2
	NGRIP	0.2	Linear from 0 to 0.5	0.2
Test 5 (AICC2023)	**EDC**	**0.1 (data) or 0.2 (no data)**	**Linear from 0 to 0.5**	**0.2**
	EDML	**0.1 (data) or 0.2 (no data)**	**Linear from 0 to 1**	**0.2**
	VK	**0.1 (data) or 0.2 (no data)**	**Linear from 0 to 0.5**	**Linear from 0.2 to 0.7**
	TALDICE	**0.2**	**Linear from 0 to 1**	**0.2**
	NGRIP	**0.2**	**Linear from 0 to 0.5**	**0.2**

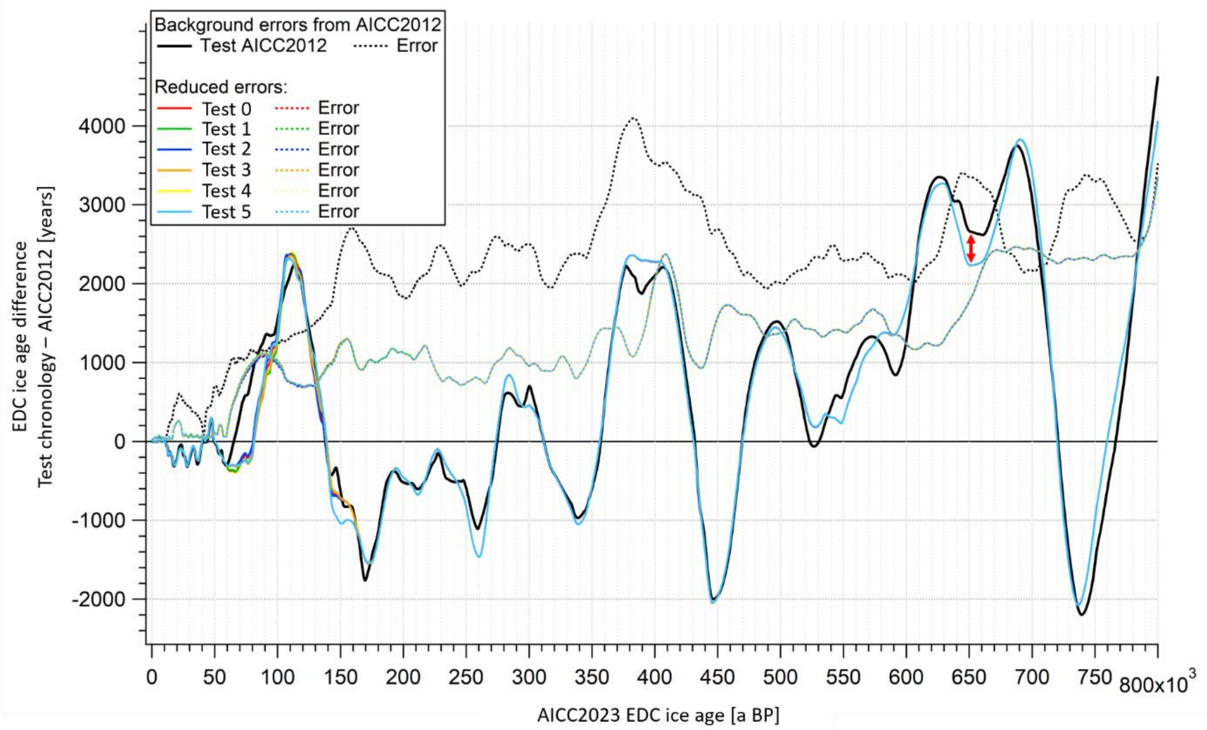

Figure S8. EDC ice age difference between each test chronology and AICC2012 timescale between 800 and 0 ka BP. The ice age uncertainty (1σ) obtained for each test is shown by the dotted lines. The red arrow indicates the largest age mismatch between the test chronologies.

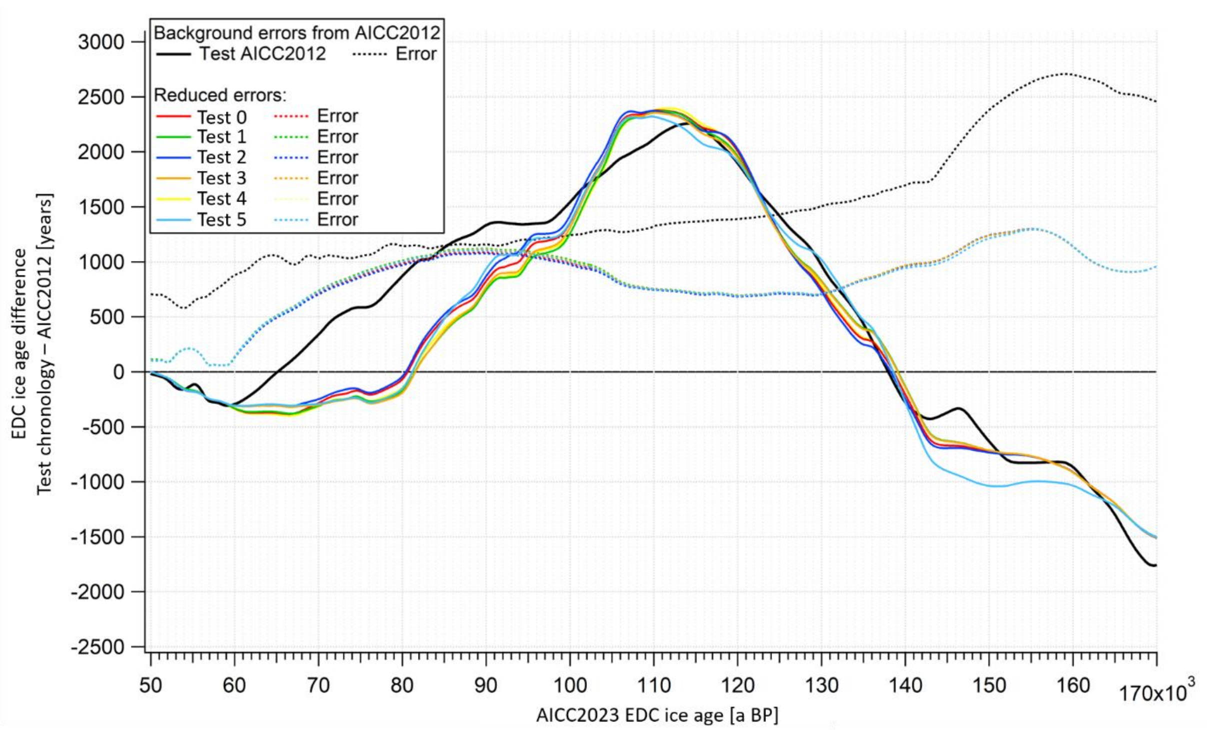

Figure S9. EDC ice age difference between each test chronology and AICC2012 timescale between 170 and 50 ka BP. The ice age uncertainty (1σ) obtained for each test is shown by dotted lines.

4 The new AICC2023 chronology

4.1 New age constraints

4.1.1 $\delta^{18}O_{atm}$, $\delta O_2/N_2$ and TAC age constraints for EDC

Table S5. $\delta^{18}O_{atm}$, $\delta O_2/N_2$ and TAC age constraints used for EDC in AICC2023. Sources: A (this work), B (Bazin et al., 2013) and C (Extier et al., 2018a).

$\delta^{18}O_{atm}$				$\delta O_2/N_2$				TAC			
EDC depth (m)	Gas age (ka BP)	Uncertainty (years)	Source	EDC depth (m)	Ice age (ka BP)	Uncertainty (years)	Source	EDC depth (m)	Ice age (ka BP)	Uncertainty (years)	Source
1465.61	108.50	1303.84	C	1495.96	117.4	3000	A	645.31	30.95	3000	A
1585.2	120.90	1303.84	C	1652.39	125.8	3000	A	782.86	47.95	3000	A
1706.92	128.80	1303.84	C	1772.83	138.1	3000	A	1337.51	93.85	3000	A
1903.01	160.40	1860.11	C	1823.08	150.1	3000	A	1453.56	107.15	3000	A
1921.37	163.00	1860.11	C	1915.39	164.6	3000	A	1588.23	118.35	3000	A
1931.13	165.20	1860.11	C	1964.71	176	3000	A	1650.52	124.75	3000	A
1997.19	178.30	1860.11	C	2008.15	187.2	3000	A	1747.64	135.95	3000	A
2050.18	191.80	2282.54	C	2065.72	196.8	3000	A	1853.73	150.05	3000	A
2096.02	199.00	2282.54	C	2128.92	210.1	3000	A	1938.82	165.35	3000	A
2139.91	207.90	2282.54	C	2196.61	220.8	3000	A	2121.53	210.05	3000	A
2160.01	209.3	2282.54	A	2232.66	231.7	3000	A	2205.70	222.85	3000	A
2229.99	225.3	1303.84	C	2281.09	240.1	3000	A	2237.52	230.45	3000	A
2232.88	227.60	1253	A	2336.71	253.4	3000	A	2274.72	238.9	3000	A
2258.68	233.2	1486.61	A	2374.24	268	3000	A	2318.83	252.55	3000	A
2300.06	242.20	1140.18	C	2406.67	281.1	3000	A	2383.34	268.95	3000	A
2332.74	248.4	1140.18	A	2438.00	290.4	3000	A	2505.82	313.35	3000	A
2363.62	258.70	1140.18	C	2469.99	302.2	3000	A	2623.99	353.65	3000	A
2376.66	264.40	1140.18	C	2502.46	312.8	3000	A	2633.73	362.125	3000	A
2409.39	279.00	2459.67	C	2536.47	325.1	3000	A	2759.45	417.15	6000	A
2451.16	289.00	2459.67	C	2572.12	334.6	3000	A	2792.11	434.15	6000	A
2466.27	293.90	2459.67	C	2603.71	344.2	3000	A	2815.91	467.05	6000	A
2475.81	301.30	1941.65	C	2622.61	354.1	6000	A	2823.81	475.4	6000	A
2490.37	304.90	1941.65	C	2639.97	366.6	6000	A	2831.30	483.55	3000	A
2522.11	316.60	1303.84	C	2677.69	372.5	6000	A	2850.57	495.45	3000	A
2582.63	334.30	1303.84	C	2685.82	377.8	6000	A	2931.35	556.25	6000	A
2599.92	337.90	1253	C	2763.95	418.1	6000	A	2962.01	569.25	6000	A
2664.62	377.30	1421.27	C	2805.78	454.9	6000	A	2986.85	578.35	6000	A
2679.89	385.70	1627.88	C	2815.83	465.7	6000	A	3000.24	587.95	6000	A
2707.22	398.50	3008.32	C	2820.37	475.4	6000	A	3013.99	599.85	3000	A
2776.91	425.9	1702.94	A	2833.08	484.2	3000	A	3020.93	611.65	3000	A
2784.70	428.8	1702.94	A	2849.73	496	3000	A	3029.38	621.55	3000	A

2791.70	434.5	1702.94	A
2793.91	440.3	1702.94	A
2838.23	483.90	4632.49	C
2857.55	500.60	4632.49	C
2873.92	504.10	7382.41	C
2894.57	521.00	3008.32	A
2904.64	531.3	3195.31	A
2909.14	534.90	3195.31	C
2917.53	549.10	4245	C
2930.36	555.60	4341.66	C
2937.72	559.10	3668.79	C
3002.71	583.00	4632.49	C
3009.86	590.00	4341.66	C
3018.09	602.7	5805.17	C
3017.25	605.08	6000	A
3027.54	615.88	6000	A
3027.9	615.20	8471.72	C
3035.41	622.07	6000	B
3038.00	627.5	6888.4	C
3040.00	633	6888.4	C
3043.01	634.42	6000	B
3043.26	638.2	7481.31	C
3048.51	649.06	6000	B
3056.77	660.79	6000	B
3065.93	676.70	6000	A
3077.74	687.33	6000	A
3093.51	698.16	6000	A
3112.43	708.96	6000	A
3119.57	714.37	6000	B
3124.27	729.38	6000	A
3131.02	733.95	6000	B
3143.2	741.94	6000	B
3152.25	754.18	6000	A
3158.91	763.07	6000	A
3166.87	772.68	6000	A
3174.81	782.61	6000	A
3180.6	797.74	6000	B
3189.83	802.46	6000	A

2863.56	506.5	3000	A
2880.63	517.3	3000	A
2892.99	525.5	3000	A
2914.24	542.5	3000	A
2929.86	556.2	3000	A
2951.86	568.4	3000	A
2986.64	577.8	3000	A
3003.49	589.5	3000	A
3013.24	599.3	3000	A
3021.40	611.3	3000	A
3029.95	620.6	3000	A
3039.12	631.7	6000	A
3043.84	644.8	6000	A
3052.27	660.7	10000	A
3059.61	671.7	10000	A
3065.69	682.9	10000	A
3082.61	691.9	10000	A
3101.62	703.9	10000	A
3123.67	714.4	10000	A
3133.92	724.9	10000	A
3141.52	732.5	10000	A
3148.60	742.9	10000	A
3155.83	752.1	10000	A
3160.42	758.3	10000	A
3165.19	767.7	10000	A
3172.00	778.8	10000	A
3181.00	787.5	10000	A

3035.80	629.75	3000	A
3043.28	642.85	3000	A
3068.47	682.75	10000	A
3078.07	691.55	10000	A
3094.01	703	10000	A
3120.55	715.35	10000	A
3139.92	730.75	10000	A
3148.15	742.55	10000	A
3160.38	767.45	10000	A
3169.76	779.75	10000	A
3179.04	787.75	10000	A

4.1.2 $\delta^{18}O_{atm}$ age constraints for Vostok

Following the dating approach proposed by Extier et al. (2018a), $\delta^{18}O_{atm}$ from Vostok ice core and $\delta^{18}O_{calcite}$ from Chinese speleothems (Cheng et al., 2016) are aligned using mid-slopes of their variations between 370 and 100 ka

BP (Fig. S10). To do so, the Vostok $\delta^{18}O_{atm}$ record and the Chinese $\delta^{18}O_{calcite}$ signal are linearly interpolated every 100 years, smoothed (25 points Savitzky-Golay) and extrema in their temporal derivative are aligned. 35 new tie points are identified and attached to a 1σ-uncertainty between 2.3 and 3.5 kyr. They replace the 35 age constraints obtained by aligning $\delta^{18}O_{atm}$ and delayed precession, associated with a 6 kyr 1σ-uncertainty and used to construct AICC2012.

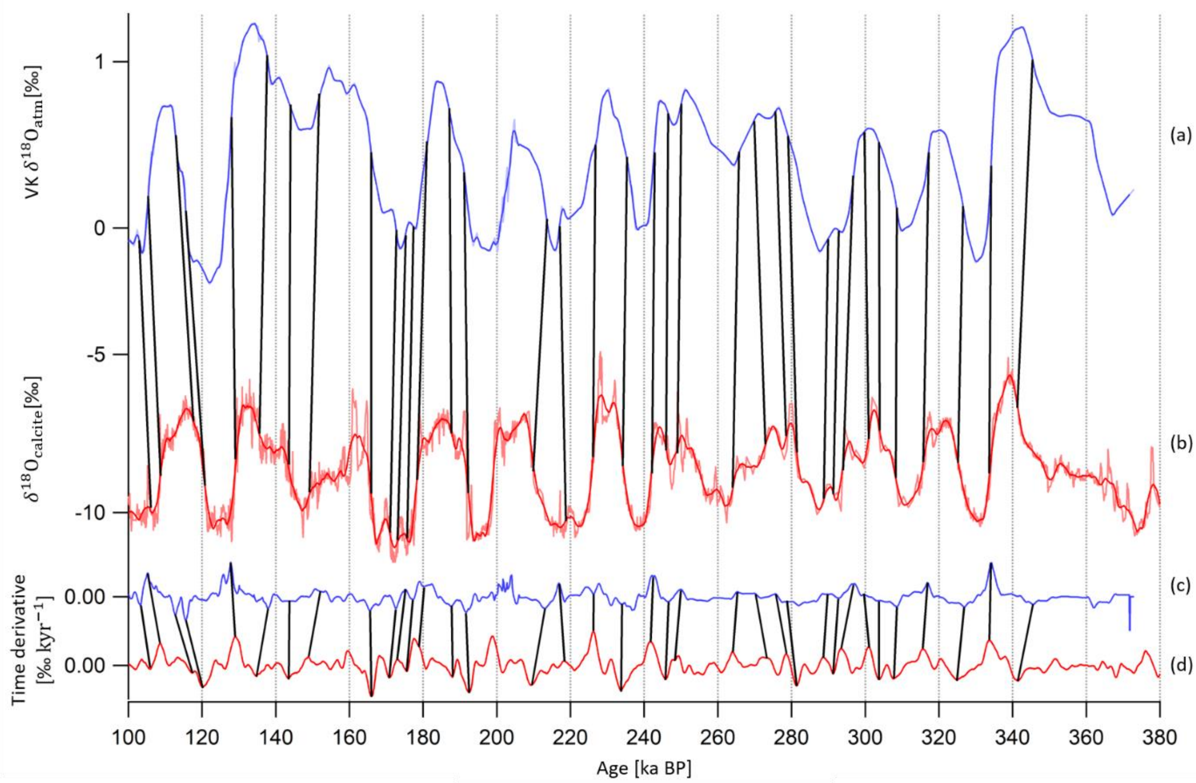

Figure S10. Alignment of Vostok $\delta^{18}O_{atm}$ and $\delta^{18}O_{calcite}$ records between 370 and 100 ka BP. (a) Vostok (VK) $\delta^{18}O_{atm}$ raw (light blue) and smoothed (dark blue, Savitzky-Golay 25 points) record (Petit et al., 1999). (b) Raw (light red) and smoothed (red) composite $\delta^{18}O_{calcite}$ from speleothems from Sambao, Hulu and Dongge caves (Cheng et al., 2016). (c) Temporal derivative of smoothed VK $\delta^{18}O_{atm}$ (blue). (d) Temporal derivative of smoothed $\delta^{18}O_{calcite}$ (red). Extrema in temporal derivatives are aligned. New tie points used to constrain AICC2023 are represented by black vertical bars.

4.2 New background scenarios

4.2.1 LID scenario for Vostok using $\delta^{15}N$ and $\delta^{40}Ar$ data

When $\delta^{15}N$ measurements are not available, Bazin et al. (2013) used a synthetic $\delta^{15}N$ signal based on the correlation between $\delta^{15}N$ and δD to estimate the background LID scenario at Vostok and to constrain the AICC2012 timescale. In this work, the background LID scenario is modified (Table S6). It is estimated from $\delta^{15}N$ data or $\delta^{40}Ar$ data (which also reflects evolution of the firn thickness) and corrected for thermal fractionation. The thermal fractionation term is estimated by the firn model running in the same configuration as for calculating the modeled LID at EDC (i.e. firn densification activation energy depending on the temperature and impurity concentration). The final LID scenario has been smoothed using a Savitzky-Golay algorithm (25 points), and then provided as an input file to Paleochrono (Fig. S11).

Table S6. Method of determination of LID background scenario according to Vostok depth range. The thermal fractionation term is estimated by the firn model running in configuration 1: Firn densification activation energy depending on the temperature and impurity concentration.

Depth range (m)	0 – 150	150 – 2737	2737 – 2847	2847 – Bottom
data availability	No	$\delta^{15}N$ (Sowers et al., 1992)	$\delta^{40}Ar$ (Caillon et al., 2003)	$\delta^{15}N$ (Sowers et al., 1992)
LID	From constant $\delta^{15}N$ (measured at 150 m) and corrected for thermal fractionation.	From $\delta^{15}N$ data, corrected for thermal fractionation and smoothed.	From $\delta^{40}Ar$ data, corrected for thermal fractionation and smoothed.	From $\delta^{15}N$ data, corrected for thermal fractionation and smoothed.

4.2.2 LID scenario for EDML using $\delta^{15}N$ data and firn model estimates

When $\delta^{15}N$ measurements are not available, Bazin et al. (2013) used a synthetic $\delta^{15}N$ signal based on the correlation between $\delta^{15}N$ and δD to estimate the background LID scenario at EDML and to constrain the AICC2012 timescale. In this work, the background LID scenario at EDML is estimated from $\delta^{15}N$ data (when available), which is corrected for thermal fractionation. The thermal fractionation term is estimated by the firn model. Otherwise, the background LID is calculated by the firn model running in the same configuration as for calculating the modeled LID at EDC (i.e. firn densification activation energy depending on the temperature and impurity concentration). The final LID scenario has been smoothed using a Savitzky-Golay algorithm (25 points), and then provided as an input file to Paleochrono (Fig. S11).

Table S7. Method of determination of LID background scenario according to EDML depth range. The thermal fractionation term is estimated by the firn model running in the same configuration as for calculating the modeled LID, i.e. firn densification activation energy depending on the temperature and impurity concentration.

Depth range (m)	0 – 548	548 – 1398.2	1398.2 – Bottom
$\delta^{15}N$ data availability	No	Yes (Landais et al., 2006)	No
LID	From constant $\delta^{15}N$ (measured at 548 m) and corrected for thermal fractionation.	From $\delta^{15}N$ data, corrected for thermal fractionation and smoothed.	From firn modeling.

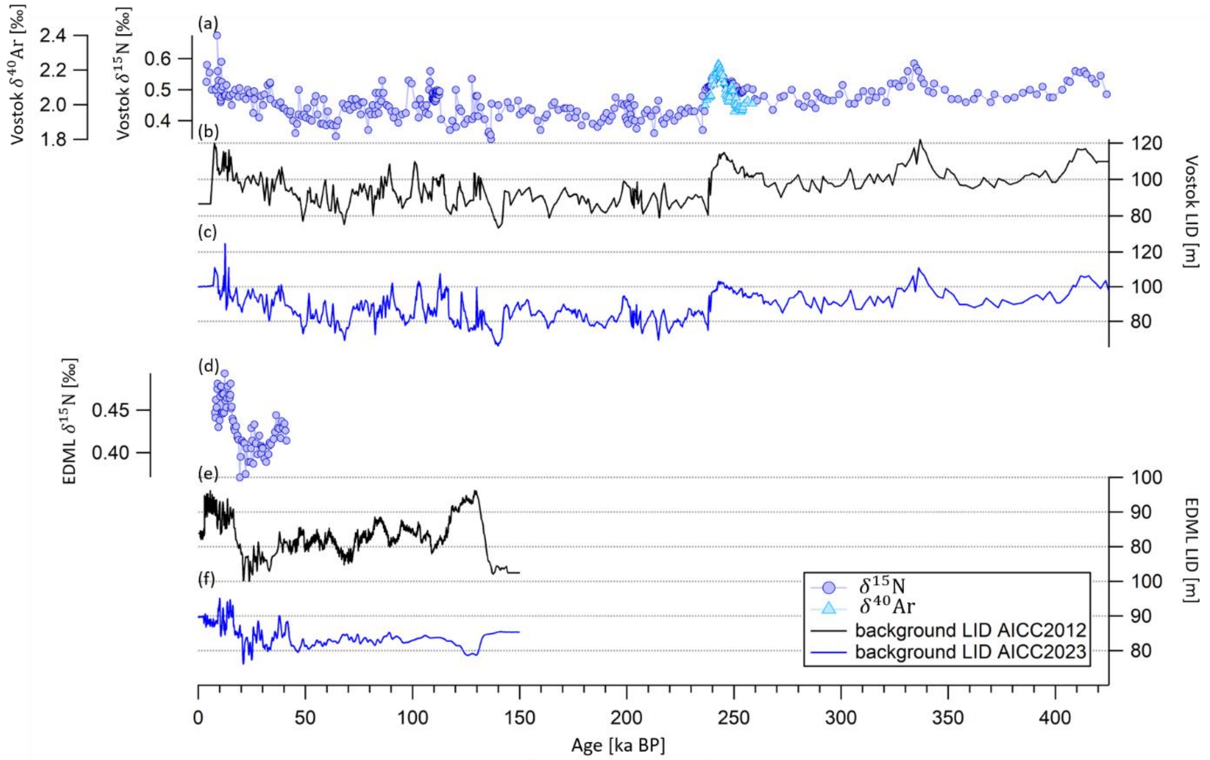

Figure S11. Records of δ^{40}Ar and δ^{15}N and LID scenarios at Vostok and EDML. (a) δ^{40}Ar and δ^{15}N records of Vostok ice core (Sowers et al., 1992; Caillon et al., 2003) and (d) δ^{15}N record of EDML ice core (Landais et al., 2006) on AICC2023 age scale. (b) Background LID at Vostok and (e) EDML used to constrain AICC2012 (Bazin et al. 2013). (c) Background LID at Vostok and (f) EDML used to constrain AICC2023 (this study).

Such modifications of the background LID scenarios have a negligible impact on the new AICC2023 chronology. Indeed, choosing the scenarios described in this section for EDML and Vostok rather than the scenarios that were used to constrain AICC2012 induces maximum age shifts of 200 and 350 years in the chronology of EDML and Vostok ice cores respectively, which is minor considering the chronological uncertainty of several hundreds of years.

4.2.3 Background scenarios and relative errors for the construction of AICC2023

With respect to the AICC2012 chronology, the background LID scenarios for EDC, Vostok, EDML and TALDICE ice cores are revised in AICC2023 (Table S8). We also reduce the background relative uncertainties associated with the LID, thinning and accumulation functions at the five sites (see Sect. 3.2 in the Supplementary Material).

Table S8. Origin of the background scenarios of LID, thinning and accumulation for EDC, EDML, Vostok, TALDICE and NGRIP and associated relative errors used in AICC2023. The LID prior relative uncertainty is set between 0.1 or 0.2 whether $\delta^{15}N$ data are available or not. The mention "AICC2012" means that the scenario is the same than in AICC2012 (Bazin et al., 2013).

	LID		**Thinning**		**Accumulation**	
	Scenario	**Relative error**	**Scenario**	**Relative error**	**Scenario**	**Relative error**
EDC	$\delta^{15}N$ Firn model	0.1 (data) 0.2 (no data)	AICC2012	Linear from 0 to 0.5	AICC2012	0.2
EDML	$\delta^{15}N$ Firn model	0.1 (data) 0.2 (no data)	AICC2012	Linear from 0 to 1	AICC2012	0.2
Vostok	$\delta^{15}N$, $\delta^{40}Ar$	0.1 (data) 0.2 (no data)	AICC2012	Linear from 0 to 0.5	AICC2012	Linear from 0.2 to 0.7
TALDICE	TALDICE-deep1 (Crotti et al., 2021) $\delta^{15}N$	0.2	AICC2012	Linear from 0 to 1	AICC2012	0.2
NGRIP	AICC2012 (Firn model)	0.2	AICC2012	Linear from 0 to 0.5	AICC2012	0.2

4.3 The new AICC2023 age scale over the last 120 kyr

With respect to the AICC2012 chronology, new stratigraphic links between ice and gas series are used to constrain AICC2023 over the past 120 kyr. They include tie points between CH_4 series from EDC, EDML, Vostok, TALDICE and NGRIP ice cores (Baumgartner et al., 2014) as well as volcanic matching points between EDC, EDML and NGRIP ice cores (Svensson et al., 2020) (Fig. S12). The gas stratigraphic links used to construct AICC2012 over the last glacial period come from matching CH_4 and $\delta^{18}O_{atm}$ variations between ice cores. Still, an offset of several centuries is observed between Antarctic and Greenland CH_4 records during the rapid increases associated with Dansgaard-Oeschger (D-O) events in AICC2012 (Fig. S12). Baumgartner et al. (2014) substantially extended the NGRIP CH_4 dataset and provided accurate tie points between NGRIP, EDML, EDC, Vostok and TALDICE CH_4 records. By implementing these new gas stratigraphic links in AICC2023, we improve the alignment between the CH_4 records by several centuries, up to 500 and 840 years for the North Atlantic abrupt warming associated with D-O 5 and 18 respectively.

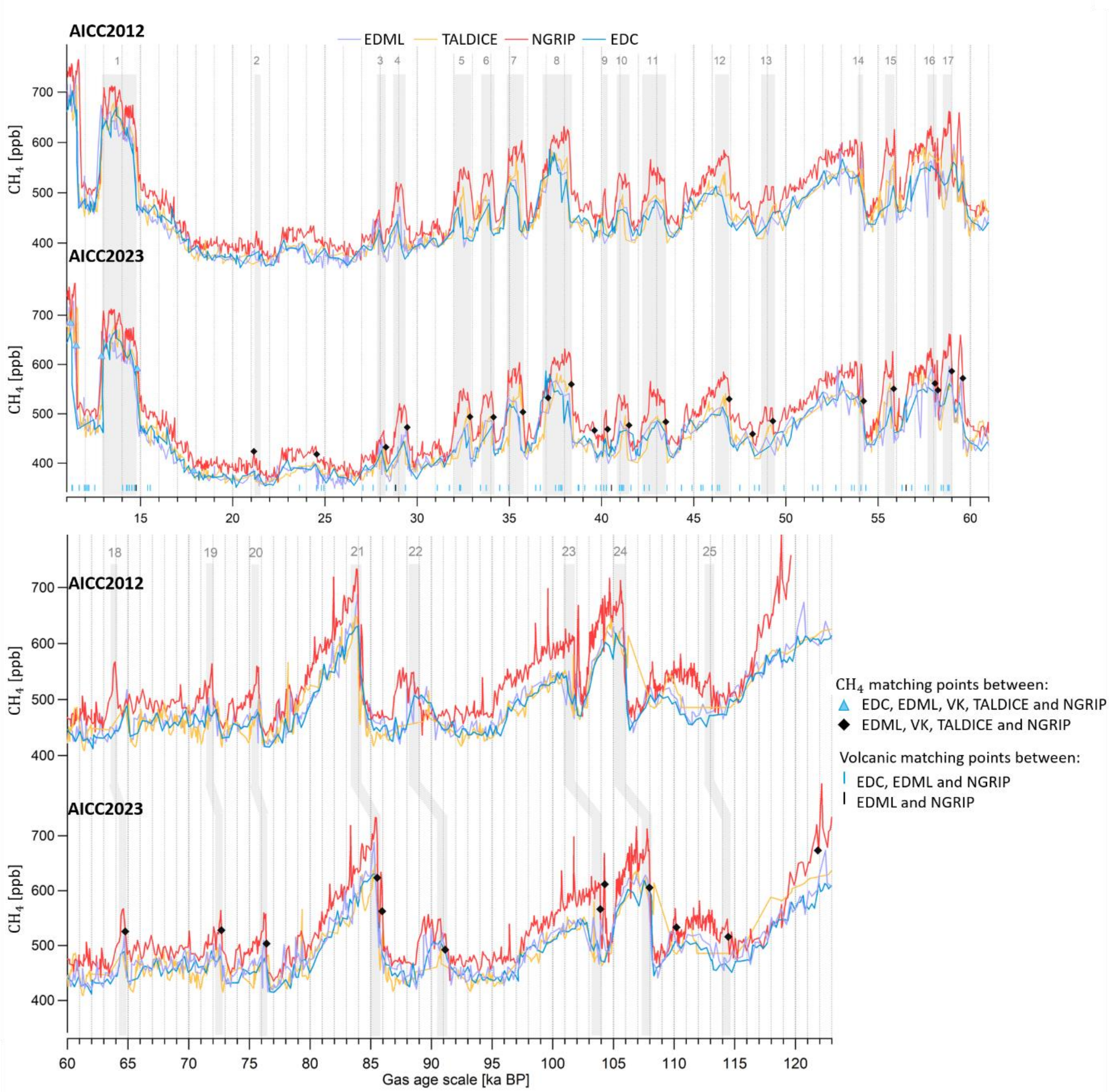

Figure S12. CH_4 records from Antarctic and NGRIP sites over the last 122 kyr. CH_4 from EDML, TALDICE, NGRIP and EDC ice cores on the AICC2012 gas timescale (top panel). CH_4 from EDML, TALDICE, NGRIP and EDC ice cores on the AICC2023 gas timescale (bottom panel). Stratigraphic links between CH_4 series from EDC, EDML, Vostok, TALDICE and NGRIP ice cores (blue triangles and black squares, Baumgartner et al., 2014) and between volcanic sulfate patterns from EDC, EDML and NGRIP ice cores (vertical bars, Svensson et al., 2020) are used to constrain AICC2023 over the last 122 kyr. Abrupt D-O events are shown by grey rectangles and numbered from the youngest to the oldest (1-25) (Barbante et al., 2006).

4.4 The new AICC2023 age scale for EDC over the last 800 kyr

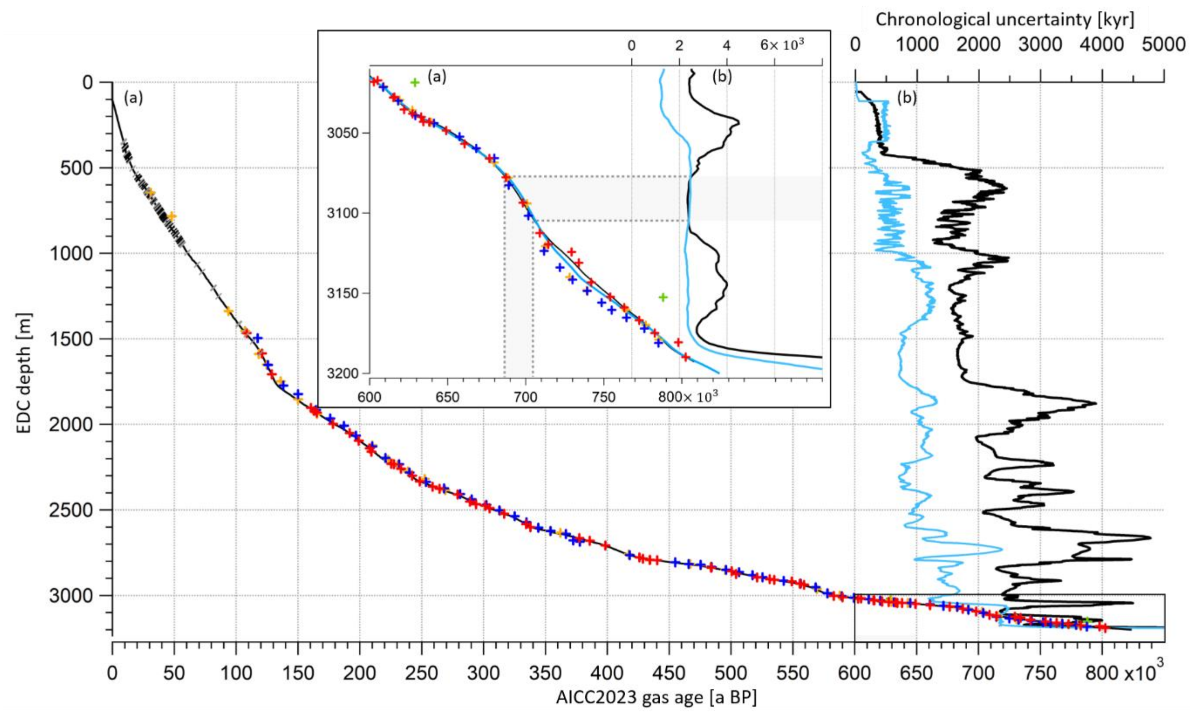

Figure S13. EDC gas age and uncertainty as a function of the depth. (a) EDC gas age (AICC2012 in black, AICC2023 in blue). (b) 1σ uncertainty (AICC2012 in black, AICC2023 in blue). Crosses and slashes represent new age constraints (ice stratigraphic links in black, gas stratigraphic links in grey, $\delta^{18}O_{atm}$ in red, $\delta O_2/N_2$ in blue, TAC in orange, ^{81}Kr in green). Inset is a zoom in between 800 and 600 ka BP. Grey rectangles frame periods where the new AICC2023 uncertainty is larger than AICC2012 uncertainty.

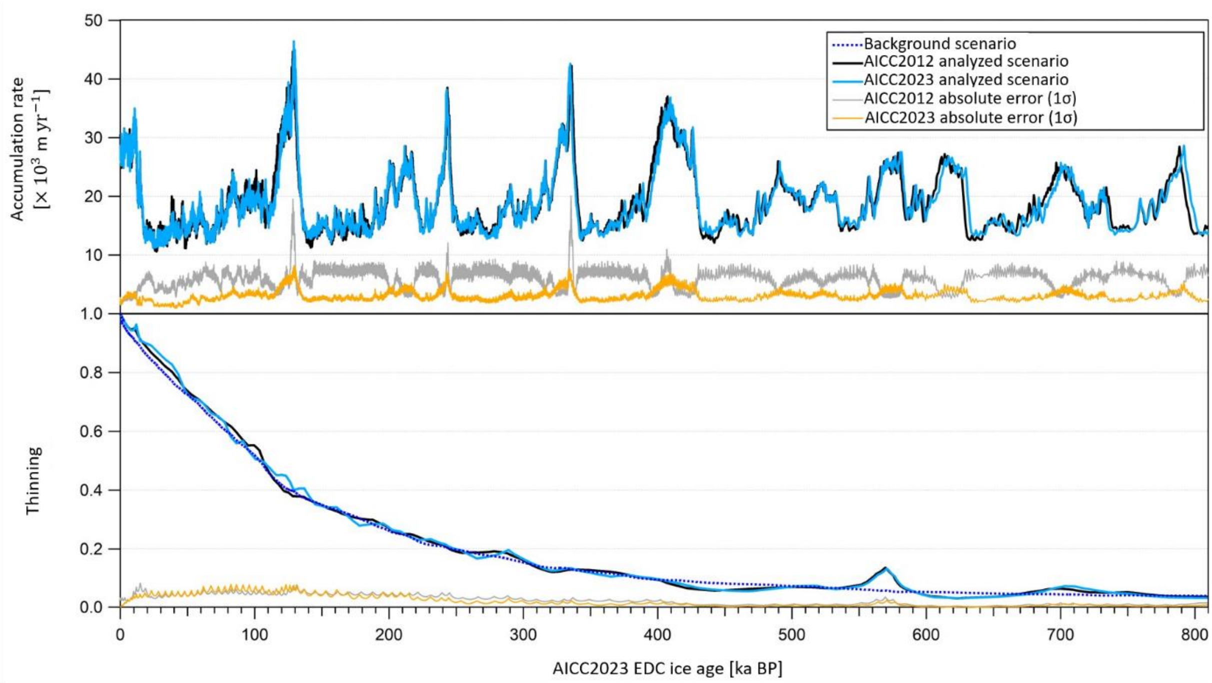

Figure S14. **Analyzed accumulation and thinning functions for EDC over the last 800 kyr.** They are provided by AICC2012 and AICC2023 (black and blue plain lines respectively) along with their absolute uncertainties (gray and yellow respectively). The background thinning function is the same for AICC2012 and AICC2023 (dark blue dotted line).

References

Barbante, C., Barnola, J.-M., Becagli, S., Beer, J., Bigler, M., Boutron, C., Blunier, T., Castellano, E., Cattani, O., Chappellaz, J., Dahl-Jensen, D., Debret, M., Delmonte, B., Dick, D., Falourd, S., Faria, S., Federer, U., Fischer, H., Freitag, J., Frenzel, A., Fritzsche, D., Fundel, F., Gabrielli, P., Gaspari, V., Gersonde, R., Graf, W., Grigoriev, D., Hamann, I., Hansson, M., Hoffmann, G., Hutterli, M. A., Huybrechts, P., Isaksson, E., Johnsen, S., Jouzel, J., Kaczmarska, M., Karlin, T., Kaufmann, P., Kipfstuhl, S., Kohno, M., Lambert, F., Lambrecht, A., Lambrecht, A., Landais, A., Lawer, G., Leuenberger, M., Littot, G., Loulergue, L., Lüthi, D., Maggi, V., Marino, F., Masson-Delmotte, V., Meyer, H., Miller, H., Mulvaney, R., Narcisi, B., Oerlemans, J., Oerter, H., Parrenin, F., Petit, J.-R., Raisbeck, G., Raynaud, D., Röthlisberger, R., Ruth, U., Rybak, O., Severi, M., Schmitt, J., Schwander, J., Siegenthaler, U., Siggaard-Andersen, M.-L., Spahni, R., Steffensen, J. P., Stenni, B., Stocker, T. F., Tison, J.-L., Traversi, R., Udisti, R., Valero-Delgado, F., van den Broeke, M. R., van de Wal, R. S. W., Wagenbach, D., Wegner, A., Weiler, K., Wilhelms, F., Winther, J.-G., Wolff, E., and Members, E. C.: One-to-one coupling of glacial climate variability in Greenland and Antarctica, Nature, 444, 195–198, DOI:10.1038/nature05301, 2006.

Barker, S., Knorr, G., Conn, S., Lordsmith, S., Newman, D., & Thornalley, D.: Early interglacial legacy of deglacial climate instability, Paleoceanogr. Paleoclimatol., 34, 1455-1475, DOI:10.1029/2019PA003661, 2019.

Barker, S., Zhang, X., Jonkers, L., Lordsmith, S., Conn, S., & Knorr, G.: Strengthening Atlantic inflow across the mid-Pleistocene transition, Paleoceanogr. Paleoclimatol., 36, DOI:10.1029/2020PA004200, 2021.

Baumgartner, M., Kindler, P., Eicher, O., Floch, G., Schilt, A., Schwander, J., Spahni, R., Capron, E., Chappellaz, J., Leuenberger, M., Fischer, H., and Stocker, T. F.: NGRIP CH4 concentration from 120 to 10 kyr before present and its relation to a δ15N temperature reconstruction from the same ice core, Clim. Past, 10, 903–920, DOI:10.5194/CP-10-903-2014, 2014.

Bazin, L., Landais, A., Lemieux-Dudon, B., Toyé Mahamadou Kele, H., Veres, D., Parrenin, F., Martinerie, P., Ritz, C., Capron, E., Lipenkov, V., Loutre, M.-F., Raynaud, D., Vinther, B., Svensson, A., Rasmussen, S. O., Severi, M., Blunier, T., Leuenberger, M., Fischer, H., Masson-Delmotte, V., Chappellaz, J., and Wolff, E.: An optimized multi-proxy, multi-site Antarctic ice and gas orbital chronology (AICC2012): 120–800 ka, Clim. Past, 9, 1715–1731, DOI:10.5194/cp-9-1715-2013, 2013.

Bazin, L., Landais, A., Capron, E., Masson-Delmotte, V., Ritz, C., Picard, G., Jouzel, J., Dumont, M., Leuenberger, M., and Prié, F.: Phase relationships between orbital forcing and the composition of air trapped in Antarctic ice cores, Clim. Past, 12, 729–748, DOI:10.5194/cp-12-729-2016, 2016.

Bréant, C., Martinerie, P., Orsi, A., Arnaud, L., and Landais, A.: Modelling firn thickness evolution during the last deglaciation: constraints on sensitivity to temperature and impurities, Clim. Past, 13, 833–853, DOI:10.5194/cp-13-833-2017, 2017.

Buizert, C.: The Ice Core Gas Age-Ice Age Difference as a Proxy for Surface Temperature, Geophys. Res. Lett., 48, e2021GL094241, DOI:10.1029/2021GL094241, 2021.

Caillon, N., Jouzel, J., Severinghaus, J. P., Chappellaz, J., and Blunier, T.: A novel method to study the phase relationship between Antarctic and Greenland climate, Geophys. Res. Lett, 30, DOI:10.1029/2003GL017838, 2003.

Crotti, I., Landais, A., Stenni, B., Bazin, L., Parrenin, F., Frezzotti, M., Ritterbusch, F., Lu, Z. T., Jiang, W., Yang, G. M., Fourré, E., Orsi, A., Jacob, R., Minster, B., Prié, F., Dreossi, G., and Barbante, C.: An extension of the TALDICE ice core age scale reaching back to MIS 10.1, Quat. Sci. Rev., 266, 107078, DOI:10.1016/J.QUASCIREV.2021.107078, 2021.

Dreyfus, G. B., Parrenin, F., Lemieux-Dudon, B., Durand, G., Masson-Delmotte, V., Jouzel, J., Barnola, J. M., Panno, L., Spahni, R., Tisserand, A., Siegenthaler, U., and Leuenberger, M.: Anomalous flow below 2700 m in the EPICA Dome C ice core detected using δ18O of atmospheric oxygen measurements, Clim. Past, 3, 341–353, DOI:10.5194/CP-3-341-2007, 2007.

Extier, T., Landais, A., Bréant, C., Prié, F., Bazin, L., Dreyfus, G., Roche, D. M., and Leuenberger, M.: On the use of δ18Oatm for ice core dating, Quat. Sci. Rev, 185, 244–257, DOI:10.1016/J.QUASCIREV.2018.02.008, 2018a.

Extier, T., Landais, A., Bréant, C., Prié, F., Bazin, L., Dreyfus, G., Roche, D. M., and Leuenberger, M. C.: δO2/N2 records between 100-800 ka from EPICA Dome C ice core, PANGAEA, DOI:10.1594/PANGAEA.887326, 2018b.

Landais, A., Barnola, J.M., Kawamura, K., Caillon, N., Delmotte, M., Van Ommen, T., Dreyfus, G., Jouzel, J., Masson-Delmotte, V., Minster, B., Freitag, J., Leuenberger, M., Schwander, J., Huber, C., Etheridge, D. and Morgan, V., Firn-air δ15N in modern polar sites and glacial–interglacial ice: a model-data mismatch during glacial periods in Antarctica?, Quat. Sci. Rev., 25, 49-62, DOI:10.1016/j.quascirev.2005.06.007, 2006.

Landais, A., Dreyfus, G., Capron, E., Pol, K., Loutre, M. F., Raynaud, D., Lipenkov, V. Y., Arnaud, L., Masson-Delmotte, V., Paillard, D., Jouzel, J., and Leuenberger, M.: Towards orbital dating of the EPICA Dome C ice core using δO2/N2, Clim. Past, 8, 191–203, DOI:10.5194/CP-8-191-2012, 2012.

Laskar, J., Robutel, P., Joutel, F., Gastineau, M., Correia, A. C. M., and Levrard, B.: A long-term numerical solution for the insolation quantities of the Earth, Astron. Astrophys, 428, 261–285, DOI:10.1051/0004-6361:20041335, 2004.

Oyabu, I., Kawamura, K., Uchida, T., Fujita, S., Kitamura, K., Hirabayashi, M., Aoki, S., Morimoto, S., Nakazawa, T., Severinghaus, J. P., and Morgan, J. D.: Fractionation of O2/N2 and Ar/N2 in the Antarctic ice sheet during bubble formation and bubble–clathrate hydrate transition from precise gas measurements of the Dome Fuji ice core, Cryosphere, 15, 5529–5555, DOI:10.5194/tc-15-5529-2021, 2021.

Oyabu, I., Kawamura, K., Buizert, C., Parrenin, F., Orsi, A., Kitamura, K., Aoki, S., and Nakazawa, T.: The Dome Fuji ice core DF2021 chronology (0–207 kyr BP), Quat. Sci. Rev., 294, 107754, DOI:10.1016/J.QUASCIREV.2022.107754, 2022.

Parrenin, F., Rémy, F., Ritz, C., Siegert, M. J., and Jouzel, J.: New modeling of the Vostok ice flow line and implication for the glaciological chronology of the Vostok ice core, J. Geophys. Res. Atmos., 109, D20102, DOI:10.1029/2004JD004561, 2004.

Parrenin, F., Dreyfus, G., Durand, G., Fujita, S., Gagliardini, O., Gillet, F., Jouze, J., Kawamura, K., Lhomme, N., Masson-Delmotte, V., Ritz, C., Schwander, J., Shoji, H., Uemura, R., Watanabe, O., and Yoshida, N.: 1-D-ice flow modelling at EPICA Dome C and Dome Fuji, East Antarctica, Clim. Past, 3, 243–259, DOI:10.5194/CP-3-243-2007, 2007.

Parrenin, F., Barker, S., Blunier, T., Chappellaz, J., Jouzel, J., Landais, A., Masson-Delmotte, V., Schwander, J., and Veres, D.: On the gas-ice depth difference (Δdepth) along the EPICA Dome C ice core, Clim. Past, 8, 1239–1255, DOI:10.5194/CP-8-1239-2012, 2012.

Petit, J. R., Jouzel, J., Raynaud, D., Barkov, N. I., Barnola, J. M., Basile, I., Bender, M., Chappellaz, J., Davis, M., Delaygue, G., Delmotte, M., Kotiyakov, V. M., Legrand, M., Lipenkov, V. Y., Lorius, C., Pépin, L., Ritz, C., Saltzman, E., and Stievenard, M.: Climate and atmospheric history of the past 420,000 years from the Vostok ice core, Antarctica, Nature, 399, 429–436, DOI:10.1038/20859, 1999.

Sowers, T., Bender, M., Raynaud, D., and Korotkevich, Y. S.: δ15N of N2 in air trapped in polar ice: A tracer of gas transport in the firn and a possible constraint on ice age-gas age differences, J. Geophys. Res. Atmos., 97, 15683–15697, DOI:10.1029/92JD01297, 1992.

Svensson, A., Dahl-Jensen, D., Steffensen, J. P., Blunier, T., Rasmussen, S. O., Vinther, B. M., Vallelonga, P., Capron, E., Gkinis, V., Cook, E., Kjær, H. A., Muscheler, R., Kipfstuhl, S., Wilhelms, F., Stocker, T. F., Fischer, H., Adolphi, F., Erhardt, T., Sigl, M., Landais, A., Parrenin, F., Buizert, C., McConnell, J. R., Severi, M., Mulvaney, R., and Bigler, M.: Bipolar volcanic synchronization of abrupt climate change in Greenland and Antarctic ice cores during the last glacial period, Clim. Past, 16, 1565–1580, DOI:10.5194/cp-16-1565-2020, 2020.